Solidification and Re-melting Phenomena During Slurry Preparation Using the RheoMetal™ Process

M. PAYANDEH, MOHSEN HADDAD SABZEVAR, A.E.W. JARFORS, and M. WESSÉN

The melting sequence of the enthalpy exchange material (EEM) and formation of a slurry in the RheoMetal™ process was investigated. The EEM was extracted and quenched, together with a portion of the slurry at different processing times before complete melting. The EEM initially increased in size/diameter due to melt freezing onto its surface, forming a *freeze-on layer*. The initial growth of this layer was followed by a period of a constant diameter of the EEM with subsequent melting and decrease of diameter. Microstructural characterization of the size and morphology of different phases in the EEM and in the freeze-on layer was made. Dendritic equiaxed grains and eutectic regions containing Si particles and Cu-bearing particles and Fe-rich particles were observed in the as-cast EEM. The freeze-on layer consisted of dendritic aluminum tilted by about 30 deg in the upstream direction, caused by the rotation of the EEM. Energy dispersion spectroscopy analysis showed that the freeze-on layer had a composition corresponding to an alloy with higher melting point than the EEM and thus shielding the EEM from the surrounding melt. Microstructural changes in the EEM showed that temperature rapidly increased to 768 K (495 °C), indicated by incipient melting of the lowest temperature melting eutectic in triple junction grain boundary regions with Al_2Cu and $Al_5Mg_8Si_6Cu_2$ phases present. As the EEM temperature increased further the binary Al-Si eutectic started to melt to form a region of a fully developed coherent mushy state. Experimental results and a thermal model indicated that as the dendrites spheroidized near to the interface at the EEM/freeze-on layer reached a mushy state with 25 pct solid fraction, coherency was lost and disintegration of the freeze-on layer took place. Subsequently, in the absence of the shielding effect from the freeze-on Layer, the EEM continued to disintegrate with a coherency limit of a solid fraction estimated to be 50 pct.

DOI: 10.1007/s11663-017-1061-2
© The Author(s) 2017. This article is an open access publication

I. INTRODUCTION

FOLLOWING Kaufman *et al.*,[1] the microstructure is the key link between material processing and the resulting component properties. Moreover, in high-temperature processes, such as casting, the ability to control the microstructure formation is possible by manipulating the solidification process by altering alloying system and temperature gradient. This allows for tailoring of the microstructure to reach the desired properties of the final product. Moreover, new types of processes such as semisolid metal (SSM) casting have potential to create new innovative tailored microstructures and therefore new improved properties of the finished components for specific applications.

Flemings and Mehrabian[2] described the formation and the effect of primary globular α-Al particles as the fundamental elements in SSM processing solidification and casting process. Moreover, Flemings[3] discovered that the main advantage of SSM casting came from rheological benefits obtained during filling. Kirkwood *et al.*[4] reviewed SSM processing and concluded that the cost for SSM casting was a predominant obstacle for further developments. However, new processes such as rheocasting process, a variant of semisolid metal (SSM) casting developed by Flemings *et al.*,[5] have shown a significant improvement in cost-effectiveness for the slurry fabrication compared to thixocasting. In this process, the melt is cooled down to fabricate a slurry, instead of heating up as in thixocasting processing. Therefore, rheocasting process shows new opportunities

M. PAYANDEH is with the Department of Materials and Manufacturing, School of Engineering, Jönköping University, 553 18, Jönköping, Sweden and also with Scania AB, 151 87, Södertälje, Sweden. Contact e-mail: mostafa.payandeh@ju.se MOHSEN HADDAD SABZEVAR is with the Department of Metallurgical and Materials Engineering, Faculty of Engineering, Ferdowsi University of Mashhad, 91775-1111, Mashhad, Iran. A.E.W. JARFORS and M. WESSÉN are with the Department of Materials and Manufacturing, School of Engineering, Jönköping University, 553 18, Jönköping, Sweden.

Manuscript submitted February 26, 2017.
Article published online August 21, 2017.

to fabricate a high-quality slurry at a higher-rate manufacturing process in a more cost-effective manner.

From metallurgical perspective, rheocasting is a multistage solidification process with the formation of non-dendritic morphologies, previously discussed by Hitchcock *et al.*[6] for twin-screw rheomoulding, Kaufmann *et al.*[7] for the SSR™ process and Nafisi and Ghomashchi[8] for the SEED process. Despite these studies, there is still lack of understanding of the slurry preparation stage and the formation of the primary α-Al particles. This lack of information is partially related to the differences in technologies and their heat extraction methods as well as application of shear force to obtain globular particles.

For instance, in processes such as GISS™ and SSR™, developed by Wannasin *et al.*[9] and Martinez,[10] respectively, an internal cooling agent is used to produce slurry. Similarly, Wessén and Cao[11] developed RheoMetal™ process (previously called Rapid Slurry Forming process) which employs an internal cooling agent to produce a high solid fraction slurry in a short time. In this process, the internal cooling agent is a rotating aluminum alloy solid body or **e**nthalpy **e**xchange **m**aterial (EEM), that melts during the slurry processing and forms high solid fraction slurry. The recent findings by Payandeh *et al.*[12] and Granath *et al.*[13,14] showed that the amount of primary α-Al phase formed in this process was far from equilibrium and could deviate up to a factor ten greater than what predicted from alloy composition and processing temperature under the assumption of Scheil segregation model.

Therefore, the melting process of the EEM and the formation of solid phase in the RheoMetal™ was investigated for different alloying systems.[12] The results revealed the formation of a *freeze-on layer*, as extra solid layer, on the surface of the rotating EEM and the subsequent partial melting and disintegration of the freeze-on layer and EEM during slurry fabrication process. However, the formation and the melting of freeze-on layer were found as critical phenomena with significant influence on slurry characteristics and process stability. Payandeh *et al.*[12] also concluded that the process of the melting is an alloy-dependent phenomena. This arises from the fact that the liquidus temperature of the freeze-on layer was higher than the liquidus temperature of the EEM and this difference is more critical with increasing in the alloying elements in the melts.

These findings suggest that the design of alloying system and also process parameters needed to be properly timed to avoid that the EEM loses its integrity before the freeze-on layer was disintegrated. However, reaching to this point required the higher understanding of the effect of alloying elements in phase formation during EEM fabrication and heat transfer and temperature distribution in the melt and the EEM during slurry fabrication process. This information can improve the prediction of melting process and thereby improve the process stability for the designing of new alloying systems and also enhance the microstructural formation during slurry fabrication.

Hence, this study aims to investigate the relationship between melting/dissolution of the EEM and the formation of primary α-Al particles in the slurry. By interrupting the process before the complete EEM melting, and extracting samples of the slurry, the evolution of EEM size and microstructural changes in the EEM during slurry formation was investigated. A numerical model, based on the energy balance between the EEM and the melt, was developed to increase our understanding of the phenomena taking place during slurry formation.

II. EXPERIMENTAL

A. *EEM Fabrication*

A commercial Al-Si-Cu alloy, EN-AC-46000, was selected, Table I, and prepared in 50-kg batches using a standard resistance furnace. EEM cylinders (20 pcs.) with a diameter of 40 mm and a height of 42 mm prepared through die casting. The EEM die was kept at room temperature by means of water cooling to create similar solidification conditions for all EEMs. The EEMs were preheated to 473 K (200 °C) before being stirred into the melt. The EEM to melt weight ratio was set to 7 pct.

B. *Slurry Formation Study*

Figure 1 illustrates the procedure used in the interrupted slurry formation experiments. The EEM stirring time and stirring speed were controlled using a *Siemens Simatic S7-200* PLC™. Approximately 2.5 kg of melt was picked in a steel ladle. The temperature of the melt before immersing the EEM was measured using a K-type thermocouple. The EEM was inserted into the melt as superheat reached 25 K (25 °C), with a rotation rate of 900 rpm. Before complete dissolution, the EEM was extracted at predetermined melt/EEM contact duration, *i.e.*, 5, 8, 12, 16, 20, and 25 seconds. The extracted EEMs were quenched in water for microstructural investigation. Immediately after each EEM was removed, a small sample from the slurry was quenched in a chill die. It should be noted that the processing conditions used in these experiments were chosen to slow down the slurry formation process to some extent,

Table I. Composition (Wt Pct) and Liquidus Temperature [K (°C)] of the Alloy Used

Alloy	Si	Fe	Cu	Mn	Mg	Zn	$T_{Eutectic}$	T_L
46000	8.3	0.55	2.5	0.35	0.3	0.64	840 K (567 °C)	880 K (607 °C)

Composition was measured using optical emission spectroscopy. Balance is aluminum.

and thereby facilitate the experiments. This was achieved by using a relatively low EEM rotation speed, as well as a Si-content which is higher than that optimal for the process. In this way, the slurry formation time was increased to more than 25 seconds compared to the 10 to 15 seconds for A356.

C. *Microstructural Evaluation and Stereological Relationship*

The microstructures of the original EEM and the quenched EEM samples as well as the corresponding quenched slurries were characterized. Cross sections of the samples were grinded and polished using standard metallographic techniques. The polished surfaces were etched using a 10 pct NaOH solution to maximize contrast between the different phases for optical microscope observation. Quantitative microstructural characterization was made using an Olympus™ optical microscope and the Olympus Stream™ image analysis system.

To distinguish between slurry particles and other secondary microstructural features, a particle size discrimination technique was used. Size measurements based on image contrast were made on at least five representative images based on area/perimeter measurements. The morphology of the particles is quantitatively measured by

$$\text{Shape Factor} = \frac{4\pi A_0}{P_0}, \qquad [1]$$

where A_0 is the particle cross-section area and P_0 is the perimeter of the particle. This value shows the roundness of a specific object in the microstructure, which varies from zero for objects having a very elongated shape (dendritic morphology) to unity for objects having a perfectly round (globular) morphology.

The composition in the regions of interest in the EEM and the slurries were evaluated using Energy Dispersive Spectroscopy (EDS) measurements in the SEM from five different regions using a fixed accelerating voltage of 15 to 20 kV.

III. RESULTS AND DISCUSSION

A. *Evolution of EEM Microstructure and Freeze-on Layer*

The evolution of shape and microstructure of the EEMs was studied by examining and comparing the as-cast EEM to the EEMs after interrupted slurry formation tests. Measurements showed an increase in EEM diameter due to the formation of a solidified layer of melt onto the EEM surface, Figure 2. This layer, the so-called *freeze-on layer*, was previously reported for different aluminum alloys by Payandeh *et al.*[12] The freeze-on layer increased in thickness up to 2.8 mm after 12 seconds immersion, followed by a period with near constant thickness up to 16 seconds. Subsequent melting/disintegration of the freeze-on layer occurred between 16 and 20 seconds after which the melting process

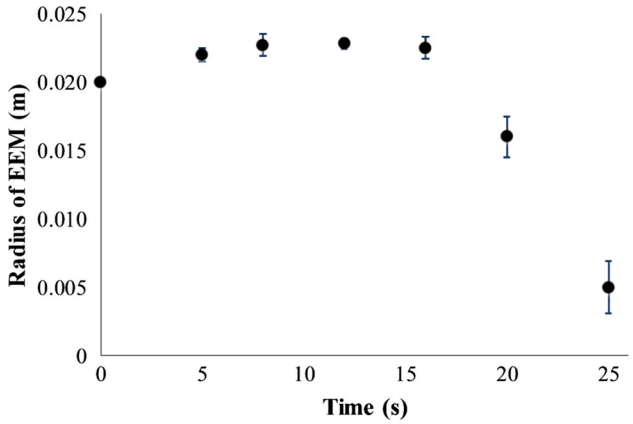

Fig. 2—The EEM radius *vs* rotational time during the slurry fabrication process.

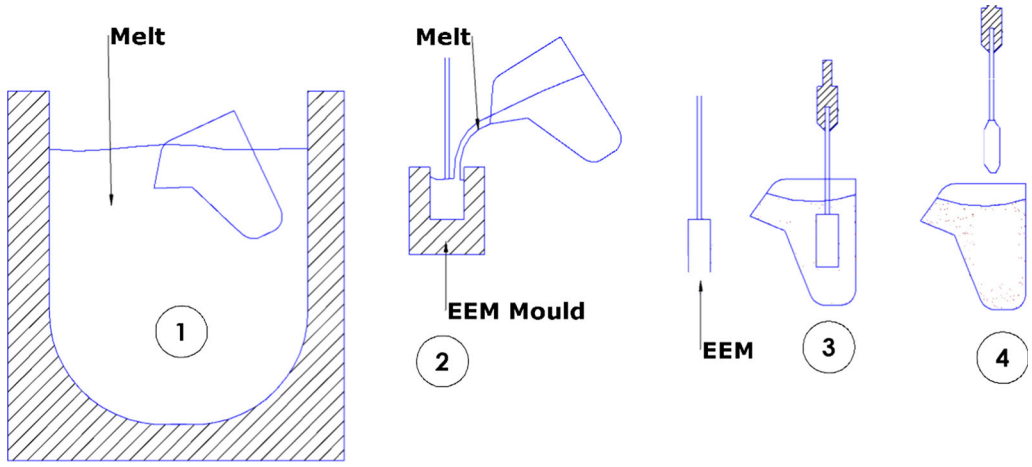

Fig. 1—The interrupted slurry formation experimental set-up; (*1*) Melt pickup from furnace, (*2*) Molding the EEM, (*3*) Immersing the EEM into the melt, (*4*) Extraction of (partially melted) EEM at different times.

accelerated and continued until 25 seconds where the average EEM radius had reduced to about 5 mm.

1. *The Microstructure in as-cast EEM*

The microstructure of the as-cast EEM was investigated, Figures 3(a) and (b). The microstructure consisted of primary aluminum dendrites and eutectic phases, Figure 3(b). EDS analysis showed that the eutectic consisted of Si particles, the Al-Cu-bearing binary compound *e.g.*, θ-Al_2Cu, $Al_5Mg_8Si_6Cu_2$ and a ternary phase containing Fe, Figures 3(c) and (d). These phases are in agreement with those predicted using

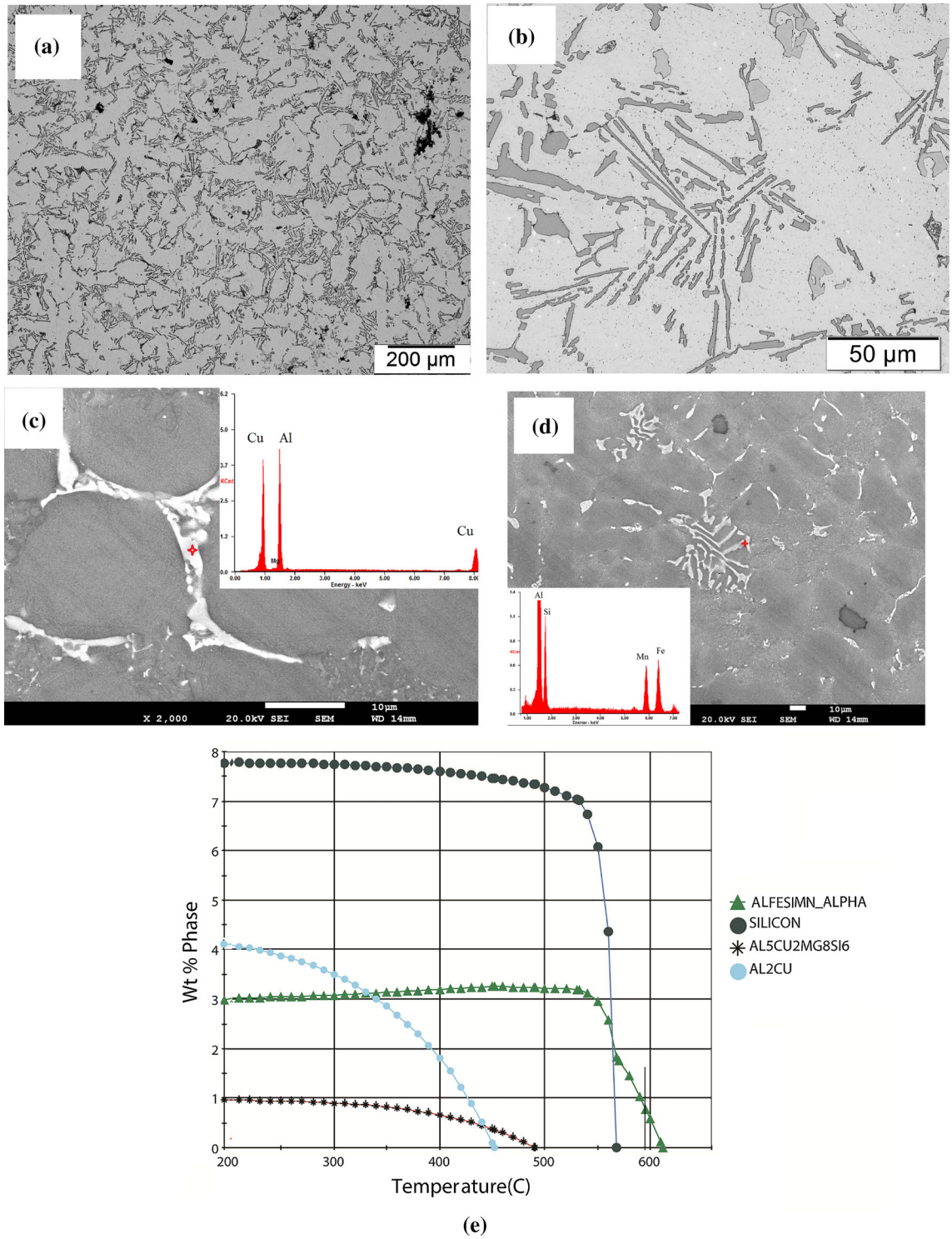

Fig. 3—(*a*) The EEM microstructure in as-cast condition average (*b*) the formation of different phases in the microstructure and EDX spectra showing (*c*) Al_2Cu and (*d*) $Al_{15}(Fe,Mn)_2Si_2$ (*e*) the modeling results from JMatPro™ showing different phases and the sequence of their formation.

JMatPro™ and the Al-DATA database developed by Saunders *et al*., Figure 3(e).[15] Measurement of the α-Al secondary dendrite arm spacing (SDAS) showed values between 20 and 30 μm. This variation affected the morphology and the size of the eutectic phases as well. Finer eutectic phases were observed in the region close to the outer parts of the EEM as compared to the center regions, as a result of higher cooling rates.

2. *Microstructure after 8 seconds*

A typical microstructure of the EEM extracted after 8 seconds is shown in Figure 4(a). The freeze-on layer microstructure is marked with "A." This layer was separated from the EEM by an air gap with a maximum thickness of 200 μm. As shown in Figure 4(b), the freeze-on layer has a columnar dendritic nature. The direction of the columnar dendrite growth was opposite to the direction of melt flow and tilted roughly 30 deg in the upstream direction, Figure 4(b). Takatani *et al*.[16] observed similar columnar dendritic grains in steel having growth selection mechanisms exhibiting ⟨100⟩ texture, tilted by about 15 deg in the presence of fluid flow.

The secondary dendritic arm spacing (SDAS) in the freeze-on layer was measured around 29 ± 4 μm. The

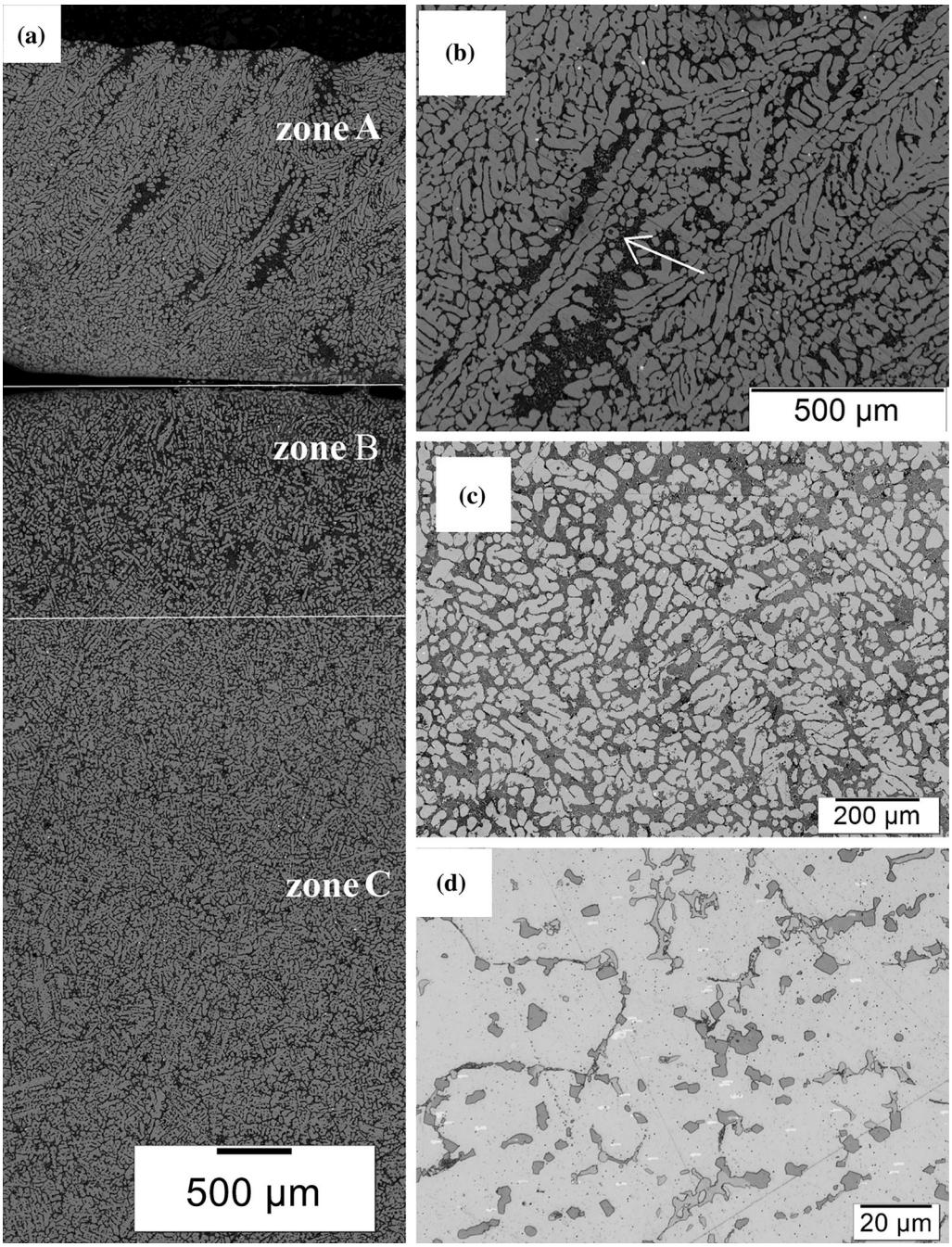

Fig. 4—(*a*) Longitudinal section showing a micrograph of the EEM after 8 s of stirring which contains three different zones (A, B, C), (*b*) Zone A as the freeze-on layer, (*c*) Zone B as the partially melted and (*d*) Zone C as the incipient melting zone.

cooling rate corresponding to this SDAS can be obtained by using an equation developed for similar aluminum alloy by Su *et al.*[17]:

$$\lambda = 50.10^{-6}\left(\frac{dT}{dt}\right)^{-0.33} \quad [2]$$

where λ(m) is secondary dendrite arm spacing and $(\frac{dT}{dt})$ (K s^{-1}) is cooling rate. The SDAS in the freeze-on layer corresponds to a cooling rate of 7.8 K s^{-1}. This corresponds to dendrite growth rate of 0.3 mm/s (0.003 m/s) for this alloy, previously reported by Sjölander.[18] As well, the measured average thickness of this layer after 8 seconds was around 0.0227 m, Figure 2, which has a good agreement with the calculated growth rate (thickness 0.024 m = 8 s × 0.003 m/s).

The eutectic phases in the freeze-on layer were studied using optical microscopy and EDS measurement, which showed that the eutectic phases were the expected α-Al, Si particles and Al_2Cu intermetallic. The microstructural investigation revealed that the amount of eutectic phases were reduced to about 50 pct compared to that of the EEM. This result was further supported by EDS measurements which revealed the freeze-on layer contained 4.65 ± 0.4 wt pct Si and 1.2 ± 0.3 wt pct Cu which is roughly half of the original melt composition. Besides, the very fine quenched morphology of the eutectic phases suggested that the eutectic region did not solidify during formation of the freeze-on layer and was probably formed at significantly higher cooling rates than the 7.8 K s^{-1} during the layer formation. It can therefore be concluded that the eutectic regions formed during the quenching of the EEM following the extraction from the melt. In addition, the deformation of dendrites caused by the shear forces can be observed in Figure 4(b) where a single bent dendrite is shown surrounded by the melt; marked by the white arrow. Therefore, this observation points to the fact that the freeze-on layer was thus in the mushy state while being subjected to the shear forces by the melt.

Moving further inwards, a layer of entrapped air was found between the freeze-on layer and the EEM, Figure 4(a). The air gap most likely formed during the immersion of the EEM into the melt. The EEM was rotating during the immersion and layer of oxides from the melt top surface and entrapped air was wrapped around the EEM, Figure 5(a). The air gap was not continuous and regions with a good contact between the EEM and freeze-on layer were also found, Figure 5(b). The regions with good contact were most likely a result of a fractured oxide layer as no traces of oxide films were observed in these regions.

During the formation of the freeze-on layer, as heat was absorbed by the EEM, the temperature increase resulted in microstructural changes inside the EEM. Considering the morphology of different phases such as shape factor of the α-Al and Al/Si eutectic phases in the extracted EEM, two distinctive zones from center to surface of EEM could be recognized, marked as "B" and "C" in Figure 4(a). Zone B and C are shown at higher magnification in Figures 4(c) and (d). A rounder morphology of α-Al phases together with a fine eutectic appeared in the zone B, Figure 4(c). The shape factor of the α-Al phase from the zone B to the zone C decreases from 0.65 ± 0.05 to 0.19 ± 0.08. The eutectic in zone B showed a significantly finer structure as compared to the original microstructure of the EEM, Figure 3. This suggests that the eutectic had at least partially melted and was rapidly solidified as the EEM was extracted from the melt and quenched.

In zone B, fragmentation and spheroidization of the equiaxed dendritic structure was found, Figure 4(c), also supporting the presence of a molten eutectic regions. According to Rettenmayr,[19] it is generally accepted that the triple grain boundaries, rich in eutectic as a consequence of microsegregation, are favorable sites for initial melting. The start of melting or incipient melting, followed by penetration of the high-energy grain boundaries, marks the start of the morphological change. Figure 6(a) shows that incipient melting took place in a grain boundary, dendrites started to fragment and multiply in the mushy region, leading to the formation of more spherical particles.

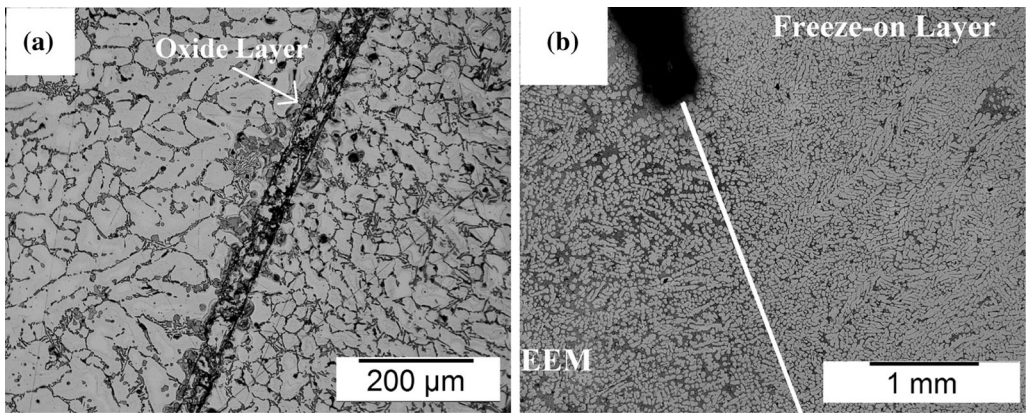

Fig. 5—The EEM/freeze-on layer interface (*a*) oxide layer (*b*) good contact between partially melted zones (zone B) in the EEM and freeze-on layer in the sample after 8 s.

Further microstructural studies of the zone C indicate that fragmentation and spheroidization of Si particles. This can be observed by studying the morphological change of the Si from needle shaped to a more spherical shape in zone C Figure 4(d), as compared to the as-cast EEM, Figure 3(b) Using higher magnification in the zone C, Figure 6(b), and comparing to the formed eutectic phases in the similar area in as-cast EEM revealed that incipient melting of regions containing some Cu-bearing particles such as $Al_5Mg_8Si_6Cu_2$ and Al_2Cu phases, took place in early stage of melting process of EEM. This was in good agreement with the melting point of these phases, which was calculated below 773 K (500 °C) using JMatPro™.

3. *Microstructure after 16 seconds*

After 16 seconds, the freeze-on layer had almost the same thickness as it had after 8 seconds suggesting that it had reached a thermal balance and was restricted by the fluid boundary layer around the rotating EEM. Microstructural investigation revealed that the morphological features, *e.g.*, the shape factor of α-Al particles in the mushy zone of EEM, zone B, were similar to those observed after 8 seconds. The thickness of this mushy zone was measured from the surface of the EEM and it was seen that the leading edge of this zone moved inward, and had almost reached the center of the EEM, Figure 7(a). Furthermore, the measurement of the amount of liquid phase at the interface between EEM and freeze-on layer showed an increasing of the phase after 16 seconds, Figure 7(b). The results revealed that 70 to 75 pct liquid phase was formed in the region very close to the interface of EEM/freeze-on layer inside the EEM. This corresponds to the eutectic fraction of this alloy according to predictions using JMatPro™ for the current alloy composition.

4. *Microstructure after 25 seconds*

The microstructure of EEM sample extracted after 25 seconds was examined. The EEM radius had reduced to only 4 to 7 mm, indicating that melting rate increased significantly after the disappearance/disintegration of the freeze-on layer. This can only be explained by an increased heat transfer to the EEM in the absence of all additional thermal resistances (freeze-on layer and airgap) with direct contact between EEM and melt. The direct contact of the EEM with the melt also induced shear forces on the EEM. It is reasonable to assume that the required liquid fraction where material loses coherency is lower, compared to a situation where

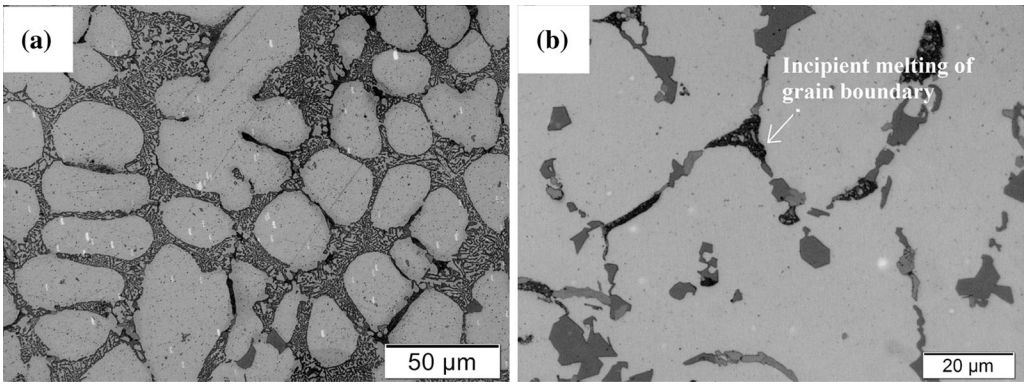

Fig. 6—(*a*) Dendrite fragmentation in the zone B and spheroidization of α-Al; (*b*) incipient melting of $Al_5Mg_8Si_6Cu_2$ and Al_2Cu intermetallic and spheroidization of intermetallic (eutectic Si, Al-Cu-bearing phase).

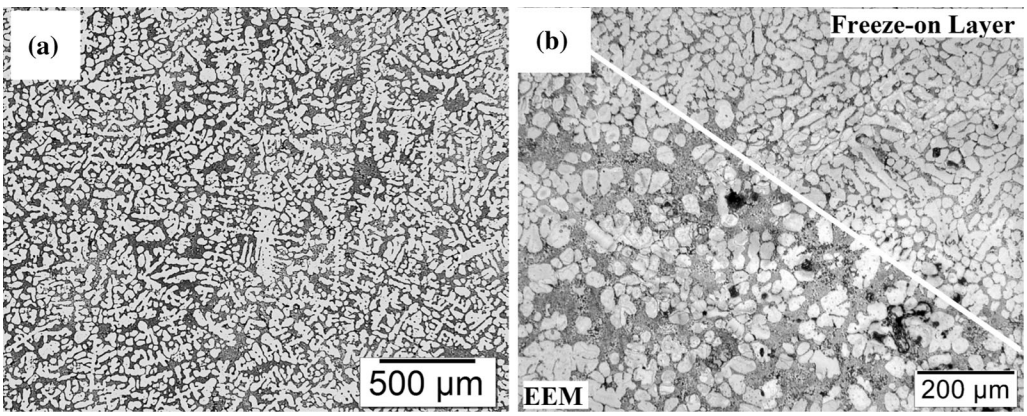

Fig. 7—(*a*) The microstructure of EEM in the center region after 16 s and (*b*) increase in amount of liquid phase in interface between EEM and freeze-on layer.

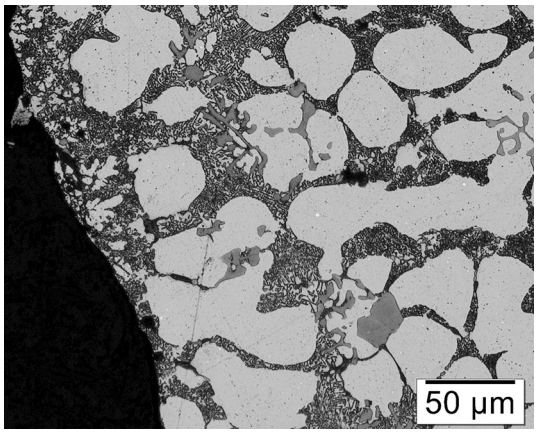

Fig. 8—The mushy zone at the EEM/melt interface in the EEM after 25 s.

the EEM is shielded by a freeze-on layer. The microstructure of EEM after 25 seconds showed that all of the eutectic phases had melted and formed a mushy zone in the entire EEM. However, the coherency of the phases still appeared high enough hinder disintegrating under the shear forces exerted by the melt. Figure 8 shows that the solid fraction is around 40 to 50 pct in the EEM near to the melt interface surface as coherency is lost.

B. *Evolution of the Slurry Microstructure*

The microstructures of slurry quenched after 8 and 25 seconds are shown in Figures 9(a) and (b), respectively. The α-Al particles, formed during stirring process, with an equiaxed rosette morphology are seen in the slurry after 8 seconds, Figure 9(a). Earlier investigation on the extracted EEM showed the formation of freeze-on layer without any evidence of dissolution of the EEM into the melt after 8 seconds. This indicated the formation of α-Al particles due to rich nucleation around the EEM after inserting into the melt. Investigation of the quenched slurry sample after 25 seconds, Figure 9(b), showed that the initial rosette/dendritic microstructure observed in Figure 9(a) had transformed into a more globular morphology due to the shearing induced by the EEM rotation. The presence of irregular and coarse primary α-Al phase implies that dendrite arms from the EEM have been fragmented and partially melted during the slurry formation.

IV. HEAT TRANSFER ANALYSIS OF THE EEM MELTING PROCESS

In the RheoMetal™ process, the exchange of thermal energy between two physical systems, the EEM (as a solid media) and the melt (as a liquid media), the rate of heat transfer depends on the properties of the materials as well as the boundary conditions between the EEM and the melt. The fundamental modes of heat transfer due to the rotation of the EEM consist of *conduction* and *convection*. Convection as the most dominant heat transfer mechanism between the EEM and the melt has a significant effect on the heat exchange. In addition, considering the likely formation of an oxide layer together with trapped air between the EEM and the freeze-on layer, the heat exchange between the solid and fluid domains becomes rather complex.

The formation of a freeze-on layer, the temperature evolution in the system, as well as the melting of the EEM were modeled. As evolution of the microstructure was related to temperature, the commercial software JMatPro™ was used for thermodynamic calculations. In order to simplify the discussion, the following nomenclature will be used: Zone A refers to the freeze-on layer; Zone B refers to the mushy zone inside the EEM as shown in Figure 4(c); and Zone C refers to the incipient melting zone, Figure 4(d).

A. *Numerical Model*

A numerical model for heat transport in a cylindrical coordinate system using the finite volume method was developed in MATLAB™, Figures 10(a) and (b). An explicit method approach was selected for obtaining numerical solutions of time-dependent heat transfer differential equations, developed by Hattel.[20] The model contains "r" as a space domain parameter with a constant mesh size 500 μm and "t" as time domain with a constant time step in the range of 1 ms. Three boundary conditions were used in the model to describe symmetry and surrounding air, Figure 10(a):

Centerline symmetry To simplify the model and to reduce computational time, a line of symmetry was considered at the center of the EEM. The centerline symmetry was set by using an equal temperature value between two adjacent nodes at the center (node 1 and node 2).

Effect of surrounding air The heat transfer with the surrounding air with an assumed temperature of 573 K (300 °C) was modeled by considering the last node (j) as an air boundary node with a constant temperature. The heat transfer from the melt to the surrounding air was defined as a series of thermal resistances:

$$\frac{1}{h_{\text{air}}} = \frac{1}{h_{\text{melt/ladle}}} + \frac{\delta_{\text{ladle}}}{k_{\text{ladle}}} + \frac{1}{h_{\text{air/ladle}}}. \qquad [3]$$

Assuming natural convection outside the ladle and almost zero speed of the melt at the inner surface of the ladle gives $h_{\text{melt/ladle}} = 1000 \frac{\text{W}}{\text{m}^2 K}$ and $h_{\text{air/ladle}} = 500 \frac{\text{W}}{\text{m}^2 K}$. Additionally, using a steel ladle with wall thickness of 2 mm gives $\frac{\delta_{\text{ladle}}}{k_{\text{ladle}}} = \frac{0.002}{100}$, and thereby a total effective heat transfer coefficient of around $300 \frac{\text{W}}{\text{m}^2 \text{K}}$ was found for heat transfer between surrounding air and the melt.

Heat transfer between melt and EEM interface(solid/liquid interface) The complexity of this boundary condition arises from the fact that two different phenomena influence the effective heat transfer coefficient in this boundary layer; the rotating EEM/melt and the formation of an oxide layer/air gap around the EEM.

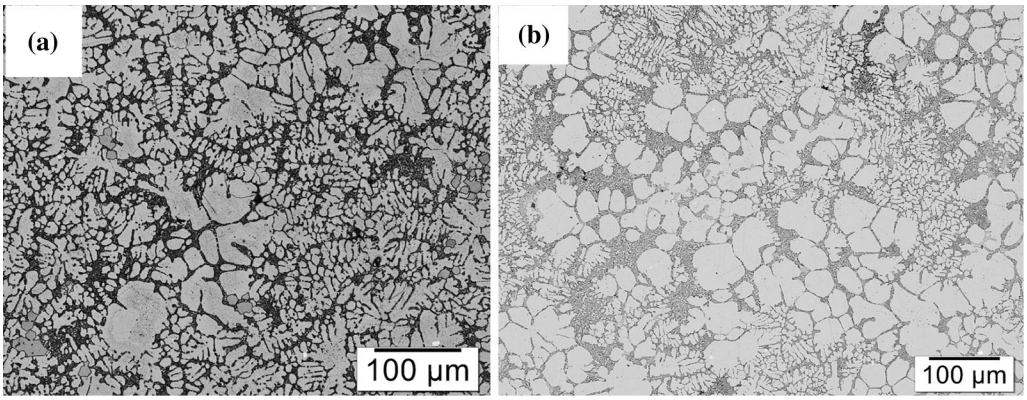

Fig. 9—Typical microstructural features of the quenched slurry samples after (*a*) 8 s and (*b*) 25 s.

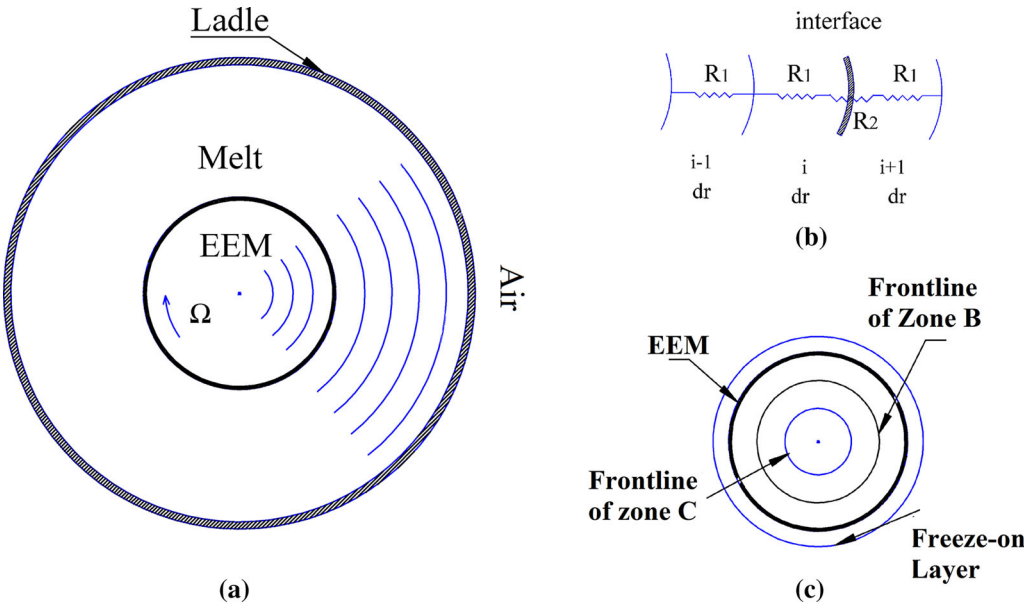

Fig. 10—(*a*) The 1D numerical model for the EEM (*b*) formulation of thermal resistance and interfaces in the model (*c*) tracing three frontlines during the simulation.

Rotational movement of the EEM as a critical phenomenon in this process must be considered by means of fluid mechanics and formulation of convective heat transfer in a rotating circular cylinder. An analytical solutions for the conductive heat transfer over an isothermal rotating cylinder for different conditions were studied by Seghir-Ouali *et al.*[21] The average heat transfer coefficient, h, for this model can be calculated based on the Nusselt number, using the Chilton-Colburn analogy, for a rotating cylinder, as given by

$$h_{\text{melt/EEM}} = \frac{Nu \times k}{D} \qquad [4]$$

and

$$\text{Nu} = 0.133\text{Re}^{0.66}\text{Pr}^{0.33}, \qquad [5]$$

where $\text{Re} = \frac{D^2\Omega}{2\nu}$ and $\text{Pr} = \frac{\nu}{\alpha}$ are the Reynolds number and Prandtl number, respectively. The process parameters D and Ω are the diameter of the EEM/freeze-on layer and the rotational velocity, respectively. The material properties k, ν, and α are the heat conductivity, viscosity, and thermal diffusivity of the melt near to the surface of EEM, respectively. This formulation gives a reasonable estimation for calculating the heat transfer coefficient, h, between EEM and melt since the calculated Reynolds number for this process is in the acceptable range for this solution (Re ~10^5). The Prandtl number, Pr, was considered in the formula since this number is very low in molten metals ($\ll 1$) and has a significant influence.

The formation of an airgap between the freeze-on layer and the EEM was treated as a heat resistivity between EEM and melt. This was done under the assumption that the effect of this resistivity was greatest in the beginning when the layer formed during immersing of EEM into the melt. The effect decreased as the thickness of the air gap reduced by considering the force from the solidified aluminum in the freeze-on layer. The

thermal resistance was calculated based on the thickness of freeze-on layer (δ) as

$$R = 200 \times 10^{-6} - 0.05 \times \delta_{\text{Freeze-onLayer}}. \quad [6]$$

Despite the assumption of 1D heat transfer in this model, neglecting the effect of heat flow from the bottom and upward through the EEM may create a considerable error in the estimation. Therefore, to account for this effect, the surface temperature of the EEM was assumed to be the same as the melt temperature and the following heat input was added to the explicit formulation at each time step:

$$Q = kA\frac{(T_{\text{melt}} - T_{\text{EEM}})}{L}dt, \quad [7]$$

where k is heat conductivity coefficient in the EEM; A is the total area of the top and bottom surfaces of the EEM, and L = 0.02 m corresponds to the height of the EEM. $(T_{\text{melt}} - T_{\text{EEM}})$ is the difference between melt temperature near to the surface of EEM and the corresponding node temperature in the EEM.

The simulation was carried out for the full slurry process duration of 25 seconds and five event horizons were traced during the simulation, as illustrated in Figure 10(c):

1. *Freeze-on layer (Zone A)* The formation of a freeze-on layer was studied during the experiment and showed that dendrites grow into the melt. According to phase formation based on JMatPro calculation, the liquidus temperature of melt, when α-Fe phase formed, was 880 K (607 °C) in this alloy. However, formation of α-Al phase occurred around 864 K (591 °C). This temperature was set as a criterion for the start of formation of a freeze-on layer.
2. *Event horizon of zone B* Formation of zone B, a mushy zone in the EEM, is important since formation of globular α-Al in the EEM takes place in this zone. This zone appeared when sufficient amounts of the eutectic melted and cause spheroidization of secondary dendritic arms. The liquid fraction at the boundary between zone B and zone C, Figure 4(a), in the EEM extracted after 8 seconds, was measured to be around 30 pct. JMatPro™, predicted the temperature corresponding to this liquid fraction to 830 K (557 °C) for this alloy, which is therefore was considered as a criterion for formation of zone B in the model.
3. *Event horizon of zone C* Formation of this zone was defined as the temperature at which the low melting point eutectic Al-Cu microconstituents start to melt (incipient melting). A temperature of 768 K (495 °C) was selected for tracing the frontline for this zone.
4. *Melting of freeze-on layer* As solidification in the freeze-on layer was assumed to take place by growth of dendrites, and further considering that this layer has a lower melting temperature than the melt, it is reasonable to assume that disintegration of this layer happens when the EEM/freeze-on layer interface loses its strength. This happens when the solid fraction of the EEM near the freeze-on layer becomes lower than the coherency point, and hence when it no longer has any mechanical strength. Therefore, melting of the freeze-on layer was related to loss of coherency of the mushy zone in the EEM. Based on experimental data, it was found that this phenomenon occurred after 16 seconds as the solid fraction reached around 25 pct at the interface of EEM/freeze-on layer. This solid fraction was set as the threshold value for freeze-on layer melting/disintegration in the model.
5. *Melting of EEM* After separation of freeze-on layer, from experimental measurement, it was estimated that the EEM melting starts when the solid fraction of frontline of EEM (EEM/melt interface) was around 50 pct solid. This was evaluated in the experiment where the EEM rotation was interrupted after 25 seconds.

B. *Alloy Thermophysical Properties*

The JMatPro™ program was used to extract alloy properties at different temperatures, Figure 11. Latent heat was added into the c_p value in model the phase transitions. The solidification/melting c_p was therefore calculated as

$$c_p^{\text{solidification/melt}} = c_p - \frac{\partial f}{\partial T}(-\Delta H) \quad [8]$$

Then the thermal diffusivity used in the Fourier heat transfer model calculated by $\alpha = \frac{k}{\rho c_p}$ in different temperatures.

The 1D heat transfer model used for this study needs to consider the EEM/melt ratio and the influence of melt rotating around the EEM. This was due to the fact that 40 nodes and 60 nodes in the model were representative of EEM and the melt "r" domain and this ratio is very much smaller than the reality where the EEM/melt weight ratio was around 7 wt pct. Otherwise, the fact that the melt had a larger mass than the EEM was neglected in the model, which results in fast solidification of the melt. Therefore, the extra mass of the melt can be inserted into the heat content (c_p value) of the nodes representing the melt domain. A non-linear function of the distance from the surface of the EEM/freeze-on layer can be applied as a correction factor according to

$$\text{Correction factor}(i) = 3r_i^{-2}, \quad [9]$$

where r_i is the radius from the center of the EEM and applied to all nodes from the surface towards the ladle.

C. *Computational Results*

The model was used to simulate the evolution of the EEM size. Due to the formation of the freeze-on layer, the EEM radius increases as in Figure 12(a), showing a similar trend as observed experimentally, Figure 2. The growth rate of the freeze-on layer at the start was estimated to be around 0.5 mm/s, which agreed well

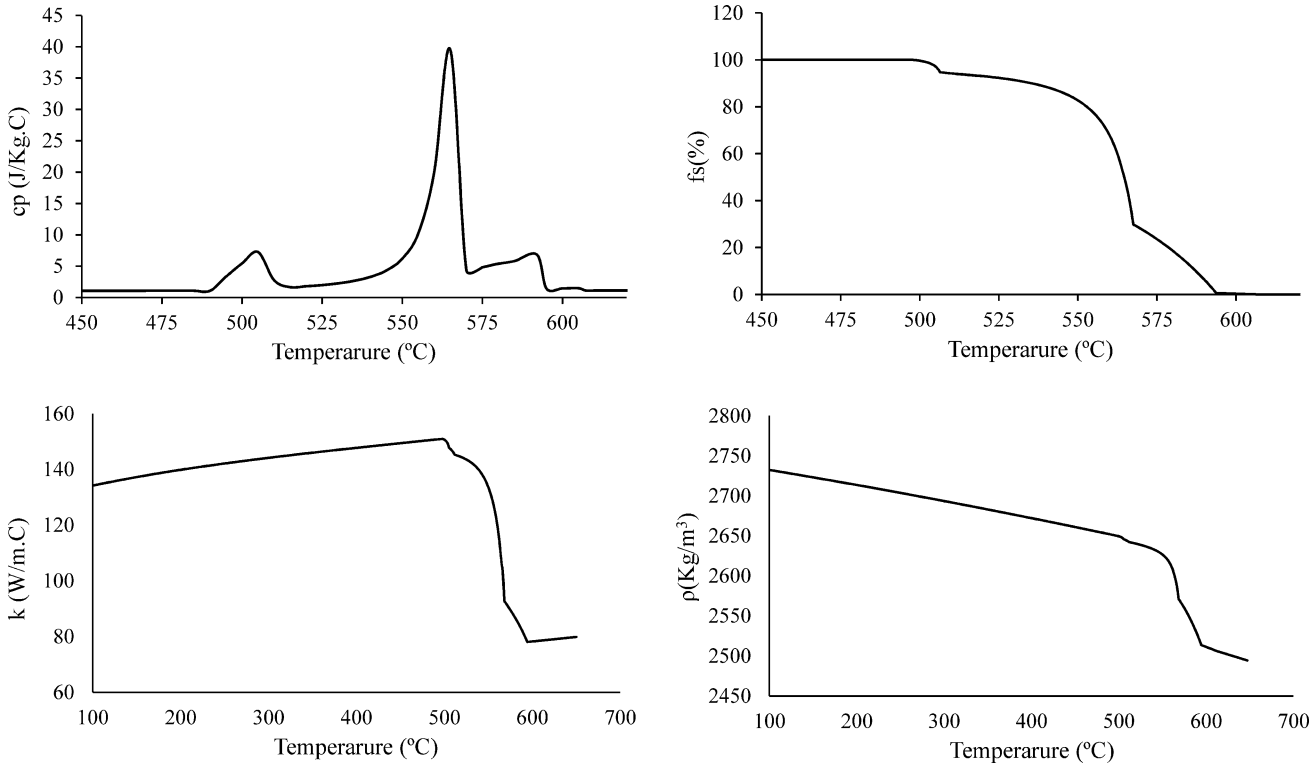

Fig. 11—Alloy properties used in the model, as extracted from JMatPro™ and the Al-DATA database.

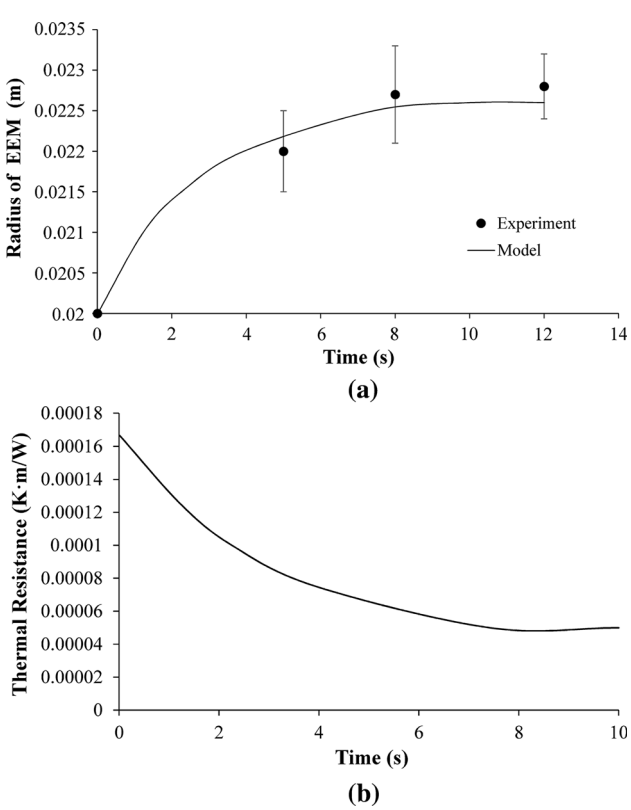

Fig. 12—Calculated profiles for the formation of the freeze-on layer during the first 10 s together with experimental data; (*b*) value for the thermal resistance between the freeze-on layer and the EEM.

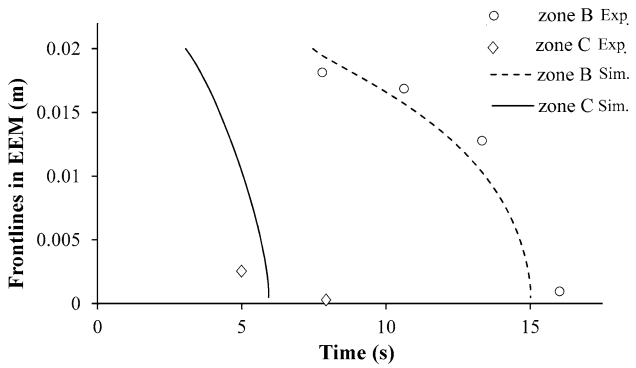

Fig. 13—The distance of the front line from the surface for zone B and zone C in the EEM.

with experimental observations of SDAS and the estimated growth rates from the EEM extracted after 8 seconds. The growth rate thereafter decreased as freeze-on layer thickness increased, and halted after 10 seconds. The average growth rate during initial stage was around 0.3 mm/s. The thermal resistivity calculated from Eq. [3] and the thickness of freeze-on layer is illustrated in Figure 12(b). As the layer formed, thermal contact between the EEM and freeze-on layer was improved by shrinkage forces and thereby the thermal resistivity was reduced.

Formation of zone B and zone C was observed in the EEM extracted after 8 seconds. The prediction of the frontline and formation of zone C in the EEM based on

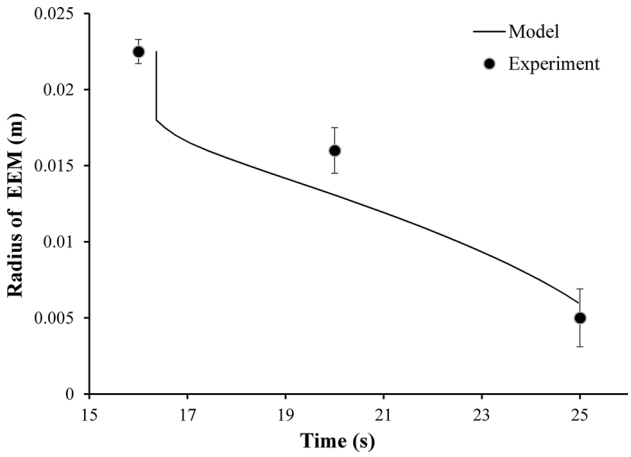

Fig. 14—Size of the EEM after 16 s showing the freeze-on layer disintegration when coherency was lost at the interface of the EEM and the freeze-on layer.

a solidus temperature of 768 K (495 °C) is shown in Figure 13. The result clearly shows that the zone C frontline progresses very rapidly into the center of the EEM as a result of heat being transferred from the superheated melt into the EEM. Zone C formed completely even before zone B started to form. This is explained by the fact that the c_p value, Figure 11, increases significantly in the temperature range of 773 K to 840 K (500 °C to 567 °C) due to phase transformations and their related heat of fusion. The formation of zone B started after 7 seconds, based on observations of the microstructure. The simulation predicted the thickness of this zone to be near to 2 mm after 8 seconds, while after 16 seconds all EEM had transferred into a mushy state. However, as this mushy zone is considered as a coherent mushy zone, the EEM keeps its rigidity even after 25 seconds.

Measurements at the interface between EEM and freeze-on layer after 16 seconds, Figure 7(b), showed that the freeze-on layer separated from the EEM when the mushy zone reached a solid fraction less than 30 pct. This solid fraction at the EEM/freeze-on layer interface becomes lower than the coherency point, when it cannot carry any loads anymore. The threshold for switching from coherent material into incoherent material can be set in the model around 25 pct, corresponding to a temperature of 945 K (672 °C). Using the above criteria, the melting curve of the freeze-on layer and EEM presents in Figure 14. The modeling results show that the separation of the freeze-on layer occurred between 16 and 17 seconds, thereafter followed by a rapid melting process. Further, the melting of the EEM itself showed reasonable agreement with experimental data; however, the size of the EEM after 20 seconds shows a lower value than that obtained experimentally.

V. CONCLUSIONS

Microstructure characteristics and chemical composition of EEMs extracted at different slurry preparation process durations using the RheoMetal™ process were investigated. The microstructural investigation showed the formation of three different zones in the initial stage of the process: a freeze-on layer, a mushy zone, and an incipient melting zone. The freeze-on layer was formed on the surface of the EEM due to rapid enthalpy exchange between the superheated melt and the cold solid EEM. This layer is characterized by growth of columnar dendrites, tilted towards the melt flow direction caused by the rotation of the EEM.

Microstructural investigation of the EEM showed that melting was initiated as the freeze-on layer started to form. The morphological change of the Si-phase as well as incipient melting of low melting point Al-Cu phase was observed after 8 seconds, which indicated that the EEM microstructure was influenced by the heat from the melt at relatively short times. This was also proven by a heat transfer model where it was shown that only 6 seconds was needed in order to reach the solidus temperature in the center of the EEM. By increasing the time of the process, the Al-Si eutectic phase starts to melt and causes the formation of globular α-Al particles due to multiplication of secondary dendritic arms. The detachment of dendrite arms and the spheroidization of these particles are suggested to be the origin of the spherical particles in the final slurry.

The melting process in RheoMetal™ process was related to coherency of the material. The heat transfer model simulated disintegration of the freeze-on layer related to the coherency of alloy at the interface of the EEM/freeze-on layer. The microstructural study together with simulation results showed that disintegration of freeze-on layer took place at a solid fraction of around 25 pct, when the material loses its capacity to carry loads. Due to shear forces from the melt acting on the EEM directly after disintegration of the freeze-on layer, the melting of EEM starts at a higher solid fraction, and thereby proceeds at a higher melting rate.

Microstructural study of the slurry as well as the EEM showed that the RheoMetal™ process is a hybrid SSM process where the non-dendritic α-Al particles were partly formed by the solidification of the melt and partly by melting process of the EEM.

ACKNOWLEDGMENTS

This work is supported by the KK-foundation (RheoCom Project No. 20100203, CompCAST 201000280), which is gratefully acknowledged. The authors would like to thank COMPtech AB for the supply of materials.

OPEN ACCESS

This article is distributed under the terms of the Creative Commons Attribution 4.0 International License (http://creativecommons.org/licenses/by/4.0/), which permits unrestricted use, distribution, and reproduction in any medium, provided you give appro-

priate credit to the original author(s) and the source, provide a link to the Creative Commons license, and indicate if changes were made.

REFERENCES

1. J.G. Kaufman, E.L. Rooy and American Foundry Society.: *Aluminum Alloy Castings: Properties, Processes, and Applications*. vol., ASM International, Materials Park, OH, 2004, pp. 61–68.
2. M.C. Flemings and R. Mehrabian: *AFS Trans.*, 1973, vol. 81, pp. 81–88.
3. M.C. Flemings: *Metall. Mater. Trans. A*, 1991, vol. 22A, pp. 957–81.
4. D.H. Kirkwood, M. Suéry, P. Kapranos, H.V. Atkinson and K.P. Young: *Semi-solid Processing of Alloys*. vol. 124, Springer, 2009.
5. M.C. Flemings, R.G. Riek, and K.P. Young: *Mater. Sci. Eng.*, 1976, vol. 25, pp. 103–17.
6. M. Hitchcock, Y. Wang, and Z. Fan: *Acta Mater.*, 2007, vol. 55 (5), pp. 1589–98.
7. H. Kaufmann, H. Wabusseg, and P.J. Uggowitzer: *Aluminium*, 2000, vol. 76 (1–2), pp. 70–75.
8. S. Nafisi and R. Ghomashchi: *Mater. Sci. Eng.: A*, 2006, vol. 437 (2), pp. 388–95.
9. J. Wannasin, R.A. Martinez, and M.C. Flemings: *Solid State Phenom.*, 2006, vol. 116, pp. 366–69.
10. R.A. Martinez, A.M., Figueredo, J.A. Yurko, M. C. Flemings, in *NADCA*, Cincinnati, OH, 2003, pp. 47–54.
11. M. Wessén and H. Cao: *In Int*, Conf. of High Tech Die Casting, Vicenza, Italy, 2006.
12. M. Payandeh, A.E.W. Jarfors, and M. Wessén: *Solid State Phenom.*, 2013, vol. 192, pp. 392–97.
13. O. Granath, M. Wessén, and H. Cao: *Int. J. Cast Metals Res.*, 2008, vol. 21 (5), pp. 349–56.
14. O. Granath, M. Wessén, and H. Cao: *In Int*, Conf. of High Tech Die Casting, Vicenza, Italy, 2006.
15. N. Saunders, U.K.Z. Guo, X. Li, A.P. Miodownik, and J.-Ph. Schillé: *JOM*, 2003, vol. 55 (12), pp. 60–65.
16. H. Takatani, C.A. Gandin, and M. Rappaz: *Acta Mater.*, 2000, vol. 48 (3), pp. 675–88.
17. S. Su, L. Moran, and EJ Lavernia: *Int. J. Rapid Solidification*, 1994, vol. 8 (3), pp. 161–77.
18. E. Sjölander: in *JTH. Research area Materials and manufacturing—Casting, Jönköping University*, Chalmers Reproservice: Göteborg, 2011, p. 45.
19. M. Rettenmayr: *Int. Mater. Rev.*, 2009, vol. 54 (1), pp. 1–17.
20. J. Hattel: *Fundamentals of Numerical Modelling of Casting Processes*. 1 ed. vol., Polyteknisk Forlag, 2005, p. 540.
21. S. Seghir-Ouali, D. Saury, S. Harmand, O. Phillipart, and D. Laloy: *Int. J. Therm. Sci.*, 2006, vol. 45 (12), pp. 1166–78.